RESEARCH ARTICLE | MAY 01 2023

Implementing microwave impedance microscopy in a dilution refrigerator **FREE**

Zhanzhi Jiang ⁽ⁱ⁾; Su Kong Chong; Peng Zhang; Peng Deng ⁽ⁱ⁾; Shizai Chu; Shahin Jahanbani ⁽ⁱ⁾; Kang L. Wang; Keji Lai ⁽ⁱ⁾

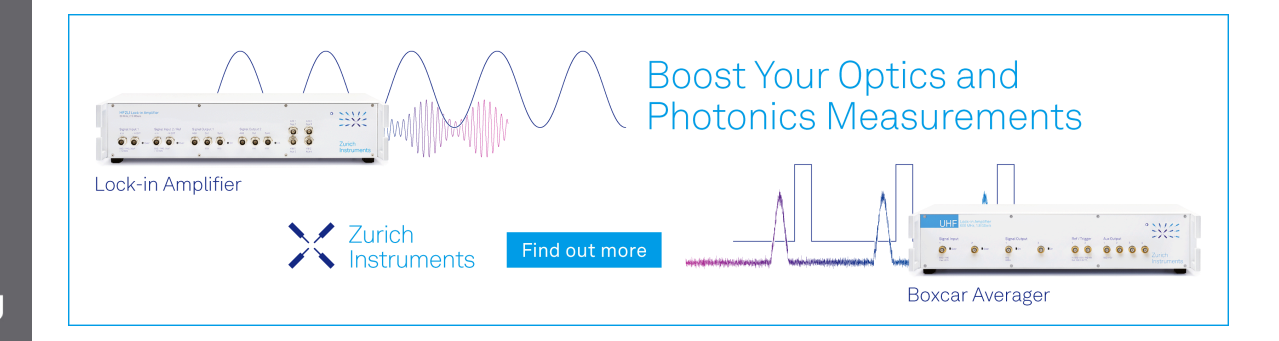


Rev. Sci. Instrum. 94, 053701 (2023) https://doi.org/10.1063/5.0138831

A CHORUS









Implementing microwave impedance microscopy in a dilution refrigerator

Cite as: Rev. Sci. Instrum. 94, 053701 (2023); doi: 10.1063/5.0138831

Submitted: 14 December 2022 • Accepted: 11 April 2023 •

Published Online: 1 May 2023







Zhanzhi Jiang,¹ D Su Kong Chong,² Peng Zhang,² Peng Deng,² D Shizai Chu,¹ Shahin Jahanbani,¹ Kang L. Wang,² and Keji Lai^{1,a)} D

AFFILIATIONS

- Department of Physics, University of Texas at Austin, Austin, Texas 78712, USA
- ²Department of Electrical and Computer Engineering, University of California, Los Angeles, California 90095, USA
- a) Author to whom correspondence should be addressed: kejilai@physics.utexas.edu

ABSTRACT

We report the implementation of a dilution refrigerator-based scanning microwave impedance microscope with a base temperature of ~ 100 mK. The vibration noise of our apparatus with tuning-fork feedback control is as low as 1 nm. Using this setup, we have demonstrated the imaging of quantum anomalous Hall states in magnetically (Cr and V) doped (Bi, Sb)₂Te₃ thin films grown on mica substrates. Both the conductive edge modes and topological phase transitions near the coercive fields of Cr- and V-doped layers are visualized in the field-dependent results. Our study establishes the experimental platform for investigating nanoscale quantum phenomena at ultralow temperatures.

Published under an exclusive license by AIP Publishing. https://doi.org/10.1063/5.0138831

I. INTRODUCTION

Near-field microwave microscopy has been an actively evolving research field in the past few decades. A wide variety of near-field probes and microwave electronics have been proposed and implemented to spatially resolve the local permittivity, permeability, conductivity, and nonlinear response of functional materials and devices. ^{1,2} For the study of quantum materials, the technique is usually configured in cryogenic environments such that the thermal energy is comparable to or smaller than the scales of intrinsic quantum mechanical energy in the system. For instance, cryogenic microwave microscopy has been demonstrated to investigate two-level quantum systems, ^{3–5} high-Tc superconductors, ^{6–10} and degenerately doped semiconductors. ¹¹ Continued effort in this field will bring much knowledge about advanced quantum systems at a length scale far below the freespace wavelength of microwave radiation.

A specific implementation of near-field microwave microscopy, microwave impedance microscopy (MIM), ¹² detects the small change in tip–sample impedance at gigahertz (GHz) frequencies, from which the nanoscale permittivity and conductivity of materials can be spatially resolved. Owing to the high spatial resolution, exquisite electrical sensitivity, and sub-surface imaging capability, the technique has found widespread applications in quantum

material research. 13,14 In the past decade, the development of cryo-MIM setups has enabled the investigation of mesoscopic quantum physics, such as correlated electronic states in complex oxides¹⁵ and moiré superlattices, ^{20–23} as well as topological edge states in semiconductor quantum wells^{24–26} and exfoliated atomically-thin layered materials. 27-31 To date, most cryo-MIM experiments have been performed in helium-4 (He4) cryostats with a base temperature (T) of 2–4K. $^{11,15-31}$ The only sub-Kelvin MIM work was carried out in a He3 refrigerator with a limited hold time and a base T of ~450 mK.32 In contrast, a He3/He4 dilution refrigerator (DR) will enable continuous operation at 100 mK or lower temperatures. The implementation of a DR-based MIM is, therefore, desirable for probing local electronic properties in ultralow-energy quantum physics, such as the fractional quantum Hall effect (FQHE)33 in semiconductor heterostructures and the quantum anomalous Hall effect (QAHE)³⁴ in magnetically doped topological insulators.

In this paper, we report the design and construction of a cryo-MIM with tuning-fork feedback control^{35,36} on a dilution refrigerator. The vibration isolation of the system is capable of keeping the topographic noise as low as ~1 nm. We demonstrate the visualization of QAHE states in magnetically (Cr and V) doped (Bi, Sb)₂Te₃ thin films grown on mica substrates at ~100 mK. Topological phase transitions near the coercive fields of Cr and V are also

observed in the field-dependent data. This work establishes the milli-Kelvin MIM platform for spatially resolving quantum phenomena at ultralow temperatures.

II. EXPERIMENTAL SETUP

The milli-Kelvin MIM is implemented in a dilution refrigerator (MNK126-500, Leiden Cryogenics, with a nominal cooling power of 500 μ W at 120 mK) inside a liquid helium dewar with an 8 T superconducting magnet. As schematically shown in Fig. 1(a), the cryostat is housed in a steel enclosure underneath the ground level. The entire structure rests on four pneumatic isolators (Micro-g Air Isolators, Technical Manufacturing Corporation) that can effectively filter out floor vibrations above 4 Hz. Two concrete boxes (not shown) are also installed to damp out vibrations from the 1K pot and still pumps. The cryostat, gas handling system, and measurement electronics are all placed inside a metal-shielded room to reduce electrical and acoustic noise from the environment.

As pictured in Fig. 1(b), the MIM module is mounted at the bottom of the mixing chamber of the DR. The module consists of the positioning and scanning stages, sample and tip holders, and a few microwave components (see below). A set of piezoelectric scanners (ANSxyz100, AttoCube Systems AG) and positioners (ANPx101 and ANPz101, AttoCube Systems AG) are stacked together to move the sample stage. At milli-Kelvin temperatures, the maximum scan window in a single frame is $30 \times 30 \mu m^2$, and the full positioning range is $3 \times 3 \text{ mm}^2$. The scan speed is kept below 100 nm/s to avoid the heating effect due to the hysteresis loss and internal friction in the piezo scanner. A pair of flexible copper braids is used as the cold finger to connect the sample stage to the mixing chamber. In our current setup, the base temperatures at the mixing chamber and at the sample stage are 60 and 100 mK, respectively. The sample temperature is mostly limited by the heat load from the piezo stacks, which are difficult to thermalize at milli-Kelvin temperatures.³⁷ While the bottom Z-positioner is in good thermal contact with the copper housing, the cooling of XY-positioners and XYZ-scanners is much less efficient. In fact, if the Teflon spacer between the sample stage and piezo scanner [as shown in Fig. 1(b)] is removed, the sample

temperature will rise to \sim 500 mK. In the future, we plan to connect all piezo stacks to the copper housing with copper wires, ³⁸ which may further reduce the sample temperature.

Figure 1(c) shows a close-up view of the tip assembly. A quartz tuning fork (ECS-.327-12.5-8X, Digikey Electronics) is used for controlling tip-sample distance and performing topography imaging. The magnetic leads of the tuning fork are replaced by non-magnetic CuNi wires to minimize magnetic effects during the field sweep. A tungsten wire with a diameter of 25 μ m is etched to a sharp tip with a radius of curvature of around 100 nm at the apex [scanning electron microscopy image in the inset of Fig. 1(c)]. The wire is then glued to one prong of the tuning fork with fast-setting epoxy (Devcon 14250). The extra mass due to the tungsten wire and glue breaks the symmetry between the two prongs and causes a shift in the resonant frequency of the tuning fork from its unloaded value of $\omega_0 = 32$ 768 Hz. On the other hand, this effect can be compensated by strain in the tungsten wire if $\Delta k/\Delta m = \omega_0^2$, where Δk and Δm are the effective spring constant and the loaded mass, respectively.³⁹ Using the Young's module of tungsten and the mass of the epoxy and tungsten wire calculated from their density and volume, we estimate that a wire length of 1–2 mm will lead to the perfect compensation between mass and strain effects. In practice, however, it is difficult to handle such a short wire with hands, and we are using a wire length of 4-5 mm for the convenience of tip gluing. With this length, the resonance frequency of the tuning fork decreases by ~500 Hz compared with ω_0 , and the estimated oscillation amplitude of its base is about 3% that of its prongs. We have found that the tuning fork stays as a good harmonic oscillator (Q = 5000-30000) at the base temperature, which is optimal for feedback control. Finally, we use a tapping amplitude of 10-30 nm in the experiment, which is much smaller than the tip diameter (100-200 nm) and does not affect the spatial

Figure 2(a) shows the schematic of tuning-fork control loops to perform topography imaging based on the frequency-modulation feedback mechanism.³⁵ We use the Nanonis BP5 SPM controller to excite the fork and regulate its response. A phase lock loop (PLL) is used to keep the tuning fork in resonance and track its resonant frequency $f_{\rm res}$. As the sample is brought into close proximity

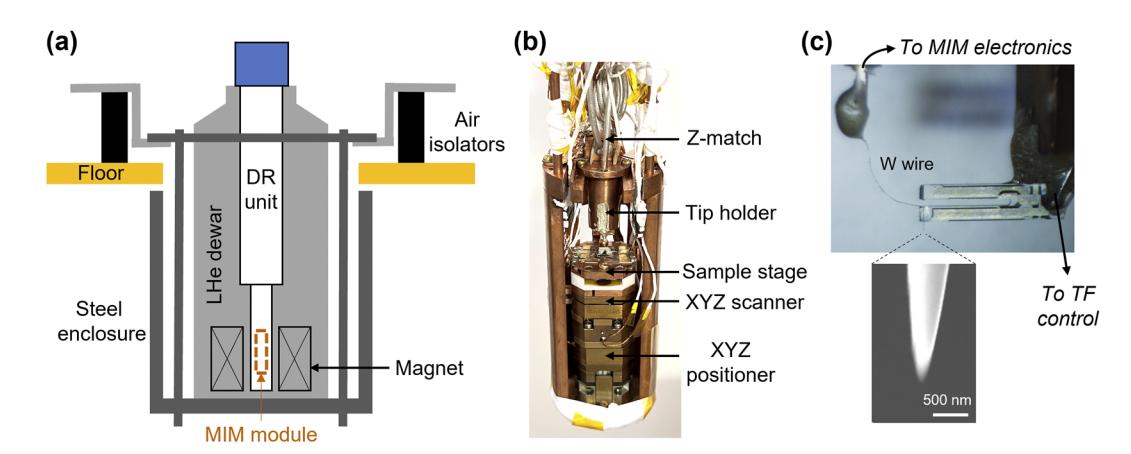


FIG. 1. (a) Schematic of the dilution refrigerator and vibration isolation. (b) Picture of the MIM module with various components. (c) Close-up view of the quartz tuning fork and a tungsten wire glued to one prong. The inset shows an SEM image of the etched tip apex.

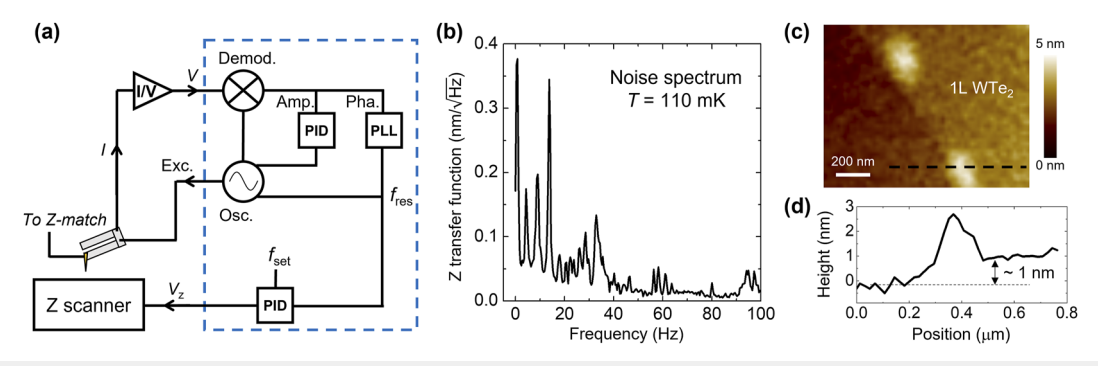


FIG. 2. (a) Schematic of the control loops for frequency-modulation-based topography imaging with the quartz tuning fork. The dashed box represents the Nanonis SPM controller. (b) Transfer function of the noise spectrum in topography imaging, showing various characteristic peaks in the *Z* noise. (c) Topographic image of a monolayer WTe₂ sample encapsulated by hBN flakes. (d) Profile along the dashed line in (c), showing the height of the monolayer as ~1 nm.

to the tip by the Z-positioner and the Z-scanner, $f_{\rm res}$ is shifted due to the tip–sample force. After the sample surface is located, a proportional–integral–differential (PID) loop regulates the height of the sample stage by controlling the Z-scanner voltage such that the frequency stays at the set point $f_{\rm set}$ as the tip is scanned across the sample. The surface topography can then be mapped out by recording the Z-scanner voltage during the raster scan. A second PID loop is also used to maintain a constant tapping amplitude for quantitative MIM experiments. As long as the Z-feedback is operating properly, we do not observe obvious tip degradation over a typical experimental window of several weeks.

The noise spectrum of the topography imaging can be obtained by holding the tip at a fixed point on the sample surface and measuring the Z transfer function (Fourier transformation of time-domain signals). As shown in Fig. 2(b), when all pumps are in operation and the sample is at the base temperature, dominant features in the noise spectrum are all below 40 Hz, as expected for the typical building vibration. Moreover, all peaks are smaller than 400 pm/ $\sqrt{\rm Hz}$, indicative of good vibration isolation in our setup. As an example of the tuning-fork performance, Fig. 2(c) shows the topographic image of a monolayer WTe₂ sample encapsulated by top and bottom hBN flakes taken at 110 mK. The line profile in Fig. 2(d) indicates that the instrument can resolve the heights of a monolayer (~1 nm) and interface bubble (~2 nm). The noise level of the DR-based MIM under working conditions is thus below 1 nm.

Figure 3 shows the configuration of microwave components inside the DR unit. Three coaxial cables-Drive, Cancel, and Output—are installed to transmit microwave signals between the DR top flange and the MIM insert. The *Drive* line sends the excitation signal to the tip through the Z-match section. The Cancel line delivers a microwave signal whose amplitude and phase are adjusted to eliminate the common-mode signal before the scanning. The signal from the tip is pre-amplified by a 30 dB cryogenic low-noise amplifier (CITLF4, Cosmic Microwave Technology)²⁴ and sent to the Output line, after which the signal is further amplified and demodulated by external microwave electronics. The two output channels are proportional to the imaginary (MIM-Im) and real (MIM-Re) parts of the tip-sample admittance.¹² Note that for tapping-mode MIM, a second demodulation at the resonant frequency of the tuning fork is needed to yield the final outputs. 35,36 The details of the MIM electronics and dual demodulation can be found in Ref. 36.

In order to balance the heat load and power transmission, we use multiple types of semi-rigid coaxial cables to construct the microwave signal lines. The section between the DR top flange and the 4K plate is made of 047 CuNi coaxial cables.³⁷ Between the 4K

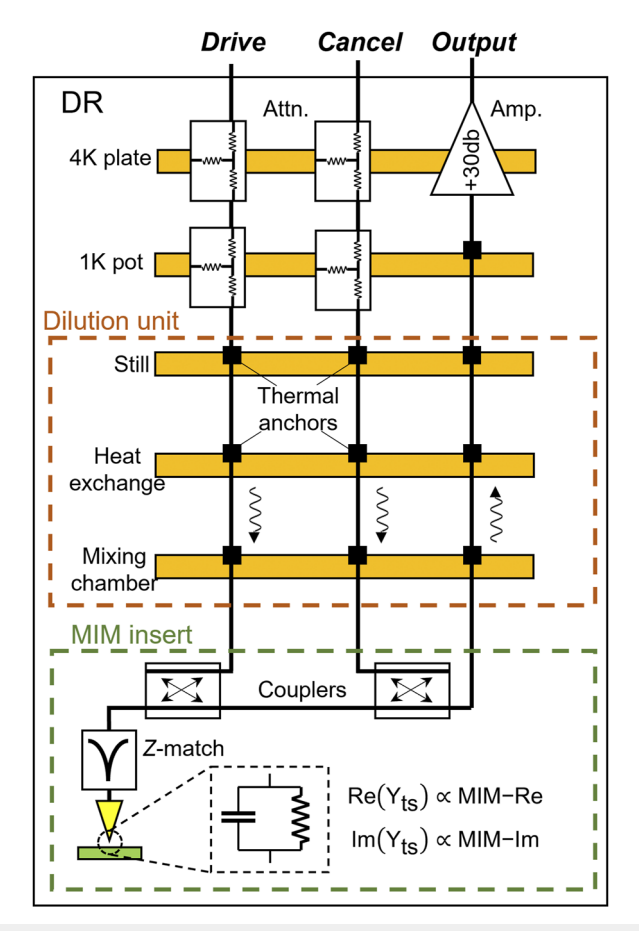


FIG. 3. Schematic of various microwave components of the MIM at different stages inside the dilution refrigerator.

plate and the mixing chamber, stainless steel cables with silver plating on the center conductor (SSS-SS 047, IntelliConnect) are used. In contrast, good thermal conductivity is desired between the mixing chamber and the tip holder, thus the usage of copper coaxial cables. On each cold plate, we install thermal anchors to thermalize the outer conductors. The cables are terminated with gold-plated CuBe or brass SubMiniature version A (SMA) connectors mounted on oxygen-free high-conductivity (OFHC) plates, which are screwed onto the cold plate. On the Drive and Cancel lines, a set of RF attenuators is installed at the 4K and 1K-pot plates to further thermalize the center conductor. According to the literature, an attenuation of 10-20 dB is needed to minimize the radiative noise from the high-T side to the low-T side of each cable.⁴⁰ In our application, however, we usually need to perform MIM measurements at various stages (room temperature, liquid nitrogen, liquid helium, and base temperature) of the cool-down process to check the tip and sample conditions. As a result, we use a modest attenuation of 3-6 dB to achieve a good balance between noise reduction and power consideration for our MIM experiment.

As shown in Fig. 3, the MIM insert is mounted at the bottom of the mixing chamber. Here, the microwave signals are routed to the Drive/Cancel/Output lines by two broadband (0.5-18 GHz) directional couplers. To ensure efficient power transfer to the tip, the excitation signal is guided to an impedance match (Z-match) section for the normal 50 Ω transmission lines. Following the design in Ref. 35, we use a 20 cm hand-formable cable with a 0.1 pF series capacitor for impedance matching. Since it is desirable to apply a tip bias in many MIM experiments, we also place a 10 M Ω chip resistor in parallel with the capacitor such that the tip can be held at a well-defined DC potential. This configuration gives a fundamental Z-match frequency of ~0.5 GHz and higher-order resonances at integer multiples of this frequency for broadband studies. For the proof-of-principle experiment below, we operate at around 2.8 GHz with a return loss of ~20 dB at the base temperature. The sensitivity of admittance (inverse impedance) detection of the MIM electronics is ~1 nS at this frequency.12

III. RESULTS AND DISCUSSIONS

We demonstrate the milli-Kelvin MIM experiment by imaging a magnetically doped topological insulator (Bi, Sb) $_2$ Te $_3$ (BST) sample grown on mica by molecular beam epitaxy (MBE). As illustrated in Fig. 4(a), the active material consists of three quintuple layers (QLs) of V-doped BST, six QLs of undoped BST, and three QLs of Cr-doped BST. 41 The heterostructure, together with a thin (~20 nm) mica layer, is exfoliated from the substrate and transferred to a heavily doped silicon wafer with 285 nm SiO $_2$ on top. The device is patterned into a standard Hall bar with Cr/Au electrodes, as shown in Fig. 4(b). Since there is no optical access to the tip–sample assembly at low temperatures, we also pattern T-shaped markers on the device in order to guide the tip toward the Hall bar.

Figures 4(c) and 4(d) show the *B*-field dependence of the Hall (σ_{xy}) and longitudinal (σ_{xx}) conductivities, respectively, at 120 mK and back-gate voltage $V_g = -30$ V. Starting from a large positive field, the quantization of σ_{xy} at $+e^2/h$ and the nearly zero σ_{xx} for fields above 1 T are clear signatures of the C = 1 QAHE state, in which the external field aligns the magnetization of both V- and Cr-doped layers. As the *B* field is swept toward the C = -1 QAHE

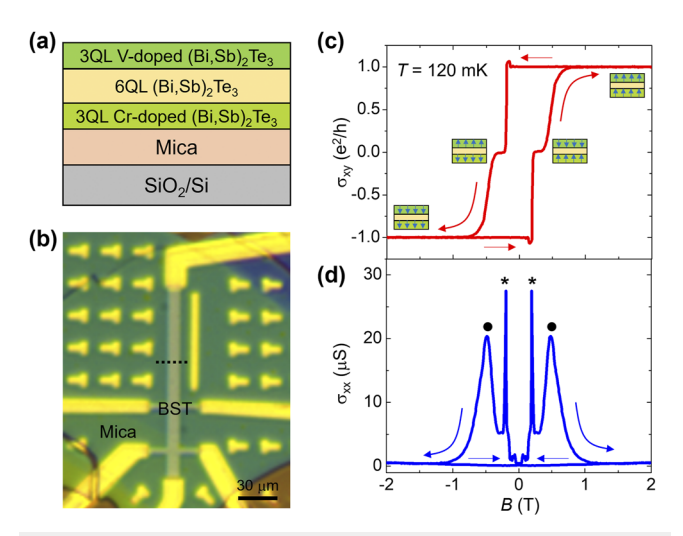


FIG. 4. (a) Cross-sectional layer structure of the sample. (b) Optical image (top view) of the Hall-bar device. (c) Magnetic field dependence of σ_{xy} and (d) σ_{xx} at T=120 mK and $V_g=-30$ V in this sample. The field is applied perpendicular to the sample surface. Arrows indicate the field sweep direction. The asterisks and dots denote the σ_{xx} peaks associated with topological phase transitions in the Cr- and V-doped BST layers, respectively.

state, two prominent σ_{xx} peaks are observed in the transport data, accompanied by two steps of change in σ_{xy} , first to zero and then to $-e^2/h$. These features are assigned to the sequential magnetization flipping of Cr- and V-doped BST layers, whose coercive fields are substantially different.⁴¹ In between the two σ_{xx} peaks, the minimum in σ_{xx} and the zero σ_{xy} plateaus indicate the formation of an axion insulator state, where the magnetization of the two doped layers is antiparallel with each other. 41 The same features occur at opposite fields as the B-field is swept from -2 to 2 T. The sweeping rate is kept at 2 mT/s such that the sample temperature is stable. We notice that neither the QAHE state nor the axion insulator state is perfect in this sample due to the presence of residual bulk carriers at $V_g = -30 \text{ V}$ (higher V_g leads to gate leakage). For the former, σ_{xx} continues to rise as increasing fields deep into the QAHE state. For the latter, the minimum in σ_{xx} does not reach zero. Further improvement in the growth procedure is, therefore, needed for a better quality sample.

The MIM results of this heterostructure device at T=130 mK are shown in Fig. 5. Since the MIM-Im signal is a monotonic function of the local conductivity, 12 we only present data from this channel for the proof of concept in this paper. The details of the MIM imaging and quantitative analysis will be reported elsewhere. Figure 5(a) displays the evolution of MIM-Im signals as the B-field is swept from 2 to -2 T along a single line across the Hall bar [dashed line in Fig. 4(b)]. 32 The characteristic line profiles at five different fields are shown in Fig. 5(b). When the system is in the C = 1 QAHE state (2 T > B > 0 T), the MIM-Im profile exhibits two prominent peaks near the physical boundaries, which is consistent with the existence of chiral edge modes under this condition. Around B = -0.08 T, the edge state disappears, and the sample is uniformly conductive. The MIM signal in the bulk drops slightly at B = -0.12 T and then increases again around B = -0.24 T. Beyond

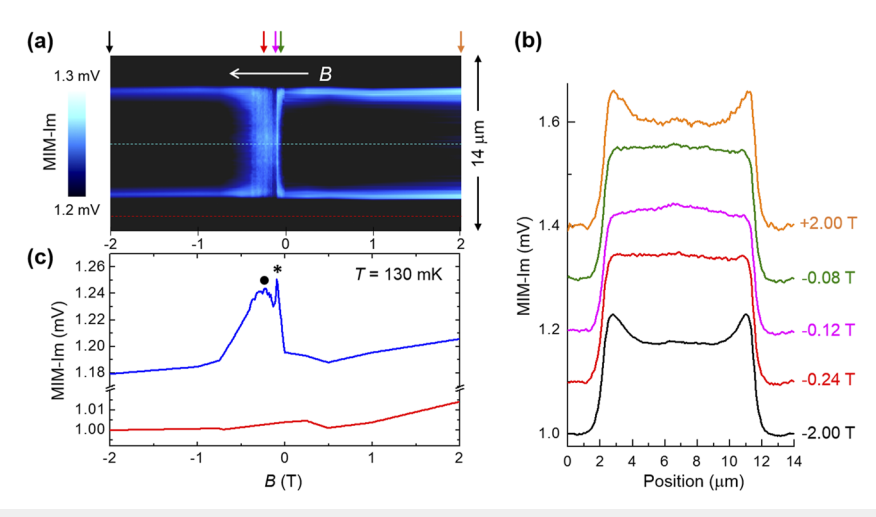


FIG. 5. (a) MIM-Im line profile along the dashed line in Fig. 4(b) as the magnetic field is swept from 2 to -2 T at 130 mK. Note that the apparent asymmetry between positive and negative fields is due to a slow background drift in the signal. (b) Selected profiles in five representative fields, as indicated by arrows in (a). The curve taken at -2.00 T corresponds to the actual MIM data. All other line cuts are offset by 0.1 mV between adjacent curves for clarity. (c) Field-dependent MIM-Im signals at the center of the Hall bar (blue curve) and on the substrate (red curve). The asterisk and dot again denote the peaks associated with the switching of Cr-doped and V-doped layers, respectively.

-1 T, the edge state reappears, as shown in the B=-2 T (C=-1 QAHE) data. The same evolution can be observed by plotting the field-dependent MIM-Im signals through the center of the sample in Fig. 5(c). Here, the narrow and broad peaks correspond to the magnetization flipping of Cr- and V-doped BST layers, respectively, and the dip between them represents the axion insulator state. The results resemble those in the σ_{xx} vs B curve obtained by the transport measurement. Note that there appears to be a background drift of the MIM signals both on the Hall bar and on the substrate [Fig. 5(c)] over this long experiment (>24 h), whose origin is subject to future studies.

Finally, we briefly discuss the milli-Kelvin MIM results on this sample. By comparing Figs. 4(d) and 5(c), one can see that the topological phase transitions occur at different fields between the transport (-0.19 T for Cr-BST and -0.48 T for V-BST) and MIM (-0.08 T for Cr-BST and -0.24 T for V-BST) data. This is presumably due to the fact that the transport experiment is performed at a much faster pace (<2 h from 2 to -2 T) than the MIM imaging (>24 h from 2 to -2 T). As a result, the phase-transition fields in the MIM measurement are closer to the actual coercive fields of the magnetically doped BST layers. In addition, the apparent edge width of $0.6-1 \mu m$ is likely due to the finite tip size and residual bulk conductance. Future experiments using sharper tips and better samples are expected to provide more accurate information on the dimension of the edge states. 42,43 Improved spatial resolution may also allow us to visualize the internal conductive edge modes along magnetic domain walls during the topological phase transitions.⁴⁴

IV. CONCLUSIONS

In summary, we have successfully implemented scanning microwave impedance microscopy in the dilution refrigerator platform with an operating temperature of $\sim \! 100$ mK. The vibration isolation in our system ensures that the topographic noise of the

tuning-fork-based sensor is below 1 nm. Using this setup, we have demonstrated the milli-Kelvin MIM imaging of quantum anomalous Hall and axion insulator states in magnetically doped (Bi, Sb) $_2$ Te $_3$ thin films. The topological phase transitions associated with magnetization switching of the Cr- and V-doped layers are seen in both transport and MIM experiments. Our study opens up new avenues for research on quantum materials in the ultralow temperature regime.

ACKNOWLEDGMENTS

This research was funded by the U.S. Department of Energy (DOE), Office of Science, Basic Energy Sciences, under Award No. DE-SC0019025. The instrumentation work was supported by the Army Research Office and accomplished under Grant Nos. W911NF-17-1-0542 and W911NF-18-1-0467. K.L.W. acknowledges support from the National Science Foundation the Quantum Leap Big Idea under Grant No. 1936383 and the U.S. Army Research Office MURI program under Grant No. W911NF-20-2-0166. The authors thank P. Wang and S. Wu for providing the WTe₂ sample and Z. Yao for sharing the equipment.

AUTHOR DECLARATIONS

Conflict of Interest

The authors have no conflicts to disclose.

Author Contributions

Zhanzhi Jiang: Conceptualization (equal); Data curation (equal); Formal analysis (equal); Writing – original draft (equal). **Su Kong Chong**: Conceptualization (equal); Data curation (equal); Writing –

review & editing (equal). Peng Zhang: Writing – review & editing (equal). Peng Deng: Writing – review & editing (supporting). Shizai Chu: Writing – review & editing (supporting). Shahin Jahanbani: Writing – review & editing (supporting). Kang L. Wang: Conceptualization (equal); Funding acquisition (equal); Supervision (equal); Validation (equal); Writing – review & editing (supporting). Keji Lai: Conceptualization (equal); Funding acquisition (equal); Supervision (equal); Writing – review & editing (lead).

DATA AVAILABILITY

The data that support the findings of this study are available from the corresponding author upon reasonable request.

REFERENCES

- ¹B. T. Rosner and D. W. van der Weide, Rev. Sci. Instrum. 73, 2505 (2002).
- ²S. M. Anlage, V. V. Talanov, and A. R. Schwartz, in *Scanning Probe Microscopy: Electrical and Electromechanical Phenomena at the Nanoscale*, edited by S. V. Kalinin and A. Gruverman (Springer, New York, 2006), pp. 207–245.
- ³S. E. de Graaf, A. V. Danilov, A. Adamyan, and S. E. Kubatkin, Rev. Sci. Instrum. 84, 023706 (2013).
- ⁴S. E. de Graaf, A. V. Danilov, and S. E. Kubatkin, Sci. Rep. 5, 17176 (2015).
- ⁵S. Geaney, D. Cox, T. Hönigl-Decrinis, R. Shaikhaidarov, S. E. Kubatkin, T. Lindström, A. V. Danilov, and S. E. de Graaf, Sci. Rep. **9**, 12539 (2019).
- ⁶I. Takeuchi, T. Wei, F. Duewer, Y. K. Yoo, X.-D. Xiang, V. Talyansky, S. P. Pai, G. J. Chen, and T. Venkatesan, Appl. Phys. Lett. 71, 2026 (1997).
- ⁷A. F. Lann, M. Abu-Teir, M. Golosovsky, D. Davidov, S. Djordjevic, N. Bontemps, and L. F. Cohen, Rev. Sci. Instrum. **70**, 4348 (1999).
- ⁸S.-C. Lee and S. M. Anlage, Appl. Phys. Lett. **82**, 1893 (2003).
- ⁹S.-C. Lee, S.-Y. Lee, and S. M. Anlage, Phys. Rev. B 72, 024527 (2005).
- ¹⁰T. Tai, B. G. Ghamsari, T. R. Bieler, T. Tan, X. X. Xi, and S. M. Anlage, Appl. Phys. Lett. **104**, 232603 (2014).
- ¹¹W. Kundhikanjana, K. Lai, M. A. Kelly, and Z.-X. Shen, Rev. Sci. Instrum. 82, 033705 (2011).
- ¹²K. Lai, W. Kundhikanjana, M. A. Kelly, and Z.-X. Shen, Appl. Nanosci. 1, 13 (2011).
- ¹³Z. Chu, L. Zheng, and K. Lai, Annu. Rev. Mater. Res. 50, 105 (2020).
- ¹⁴M. E. Barber, E. Y. Ma, and Z. X. Shen, Nat. Rev. Phys. 4, 61 (2022).
- ¹⁵ K. Lai, M. Nakamura, W. Kundhikanjana, M. Kawasaki, Y. Tokura, M. A. Kelly, and Z.-X. Shen, Science 329, 190 (2010).
- ¹⁶ W. Kundhikanjana, Z. Sheng, Y. Yang, K. Lai, E. Y. Ma, Y.-T. Cui, M. A. Kelly, M. Nakamura, M. Kawasaki, Y. Tokura, Q. Tang, K. Zhang, X. Li, and Z.-X. Shen, Phys. Rev. Lett. 115, 265701 (2015).
- ¹⁷E. Y. Ma, Y.-T. Cui, K. Ueda, S. Tang, K. Chen, N. Tamura, P. M. Wu, J. Fujioka, Y. Tokura, and Z.-X. Shen, Science 350, 538 (2015).
- ¹⁸ A. Gangshettiwar, Y. Zhu, Z. Jiang, J. Peng, Y. Wang, J. He, J. Zhou, Z. Mao, and K. Lai, Phys. Rev. B **101**, 201106(R) (2020).
- ¹⁹Q. Li, T. Miao, H. Zhang, W. Lin, W. He, Y. Zhong, L. Xiang, L. Deng, B. Ye, Q. Shi, Y. Zhu, H. Guo, W. Wang, C. Zheng, L. Yin, X. Zhou, H. Xiang, and J. Shen, Nat. Commun. 13, 6593 (2022).
- J. Shen, Nat. Commun. 13, 6593 (2022).
 Z. Chu, E. C. Regan, X. Ma, D. Wang, Z. Xu, M. I. B. Utama, K. Yumigeta, M. Blei, K. Watanabe, T. Taniguchi, S. Tongay, F. Wang, and K. Lai, Phys. Rev. Lett. 125, 186803 (2020).

- ²¹X. Huang, T. Wang, S. Miao, C. Wang, Z. Li, Z. Lian, T. Taniguchi, K. Watanabe, S. Okamoto, D. Xiao, S.-F. Shi, and Y.-T. Cui, Nat. Phys. 17, 715 (2021).
- ²²S. Miao, T. Wang, X. Huang, D. Chen, Z. Lian, C. Wang, M. Blei, T. Taniguchi, K. Watanabe, S. Tongay, Z. Wang, D. Xiao, Y.-T. Cui, and S.-F. Shi, Nat. Commun. 12, 3608 (2021).
- ²³ D. Chen, Z. Lian, X. Huang, Y. Su, M. Rashetnia, L. Ma, L. Yan, M. Blei, L. Xiang, T. Taniguchi, K. Watanabe, S. Tongay, D. Smirnov, Z. Wang, C. Zhang, Y.-T. Cui, and S.-F. Shi, Nat. Phys. 18, 1171 (2022).
- ²⁴ K. Lai, W. Kundhikanjana, M. A. Kelly, Z.-X. Shen, J. Shabani, and M. Shayegan, Phys. Rev. Lett. **107**, 176809 (2011).
- ²⁵E. Y. Ma, M. R. Calvo, J. Wang, B. Lian, M. Mühlbauer, C. Brüne, Y.-T. Cui, K. Lai, W. Kundhikanjana, Y. Yang, M. Baenninger, M. König, C. Ames, H. Buhmann, P. Leubner, L. W. Molenkamp, S.-C. Zhang, D. Goldhaber-Gordon, M. A. Kelly, and Z.-X. Shen, Nat. Commun. 6, 7252 (2015).
- ²⁶ Y.-T. Cui, B. Wen, E. Y. Ma, G. Diankov, Z. Han, F. Amet, T. Taniguchi, K. Watanabe, D. Goldhaber-Gordon, C. R. Dean, and Z.-X. Shen, Phys. Rev. Lett. 117, 186601 (2016).
- ²⁷Y. Shi, J. Kahn, B. Niu, Z. Fei, B. Sun, X. Cai, B. A. Francisco, D. Wu, Z. X. Shen, X. Xu, D. H. Cobden, and Y. Cui, Sci. Adv. 5, eaat8799 (2019).
- ²⁸W. Zhao, E. Runburg, Z. Fei, J. Mutch, P. Malinowski, B. Sun, X. Huang, D. Pesin, Y.-T. Cui, X. Xu, J.-H. Chu, and D. H. Cobden, Phys. Rev. X 11, 041034 (2021).
- ²⁹B. Sun, W. Zhao, T. Palomaki, Z. Fei, E. Runburg, P. Malinowski, X. Huang, J. Cenker, Y.-T. Cui, J.-H. Chu, X. Xu, S. S. Ataei, D. Varsano, M. Palummo, E. Molinari, M. Rontani, and D. H. Cobden, Nat. Phys. 18, 94 (2022).
- ³⁰W. Lin, Y. Feng, Y. Wang, Z. Lian, H. Li, Y. Wu, C. Liu, Y. Wang, J. Zhang, Y. Wang, X. Zhou, and J. Shen, Phys. Rev. B 105, 165411 (2022).
- ³¹ W. Lin, Y. Feng, Y. Wang, J. Zhu, Z. Lian, H. Zhang, H. Li, Y. Wu, C. Liu, Y. Wang, J. Zhang, Y. Wang, C.-Z. Chen, X. Zhou, and J. Shen, Nat. Commun. 13, 7714 (2022).
- ³² M. Allen, Y. Cui, E. Y. Ma, M. Mogi, M. Kawamura, I. C. Fulga, D. Goldhaber-Gordon, Y. Tokura, and Z.-X. Shen, Proc. Natl. Acad. Sci. U. S. A. 116, 14511 (2019).
- 33 D. C. Tsui, H. L. Stormer, and A. C. Gossard, Phys. Rev. Lett. 48, 1559 (1982).
- ³⁴C.-Z. Chang, J. Zhang, X. Feng, J. Shen, Z. Zhang, M. Guo, K. Li, Y. Ou, P. Wei, L.-L. Wang, Z.-Q. Ji, Y. Feng, S. Ji, X. Chen, J. Jia, X. Dai, Z. Fang, S.-C. Zhang, K. He, Y. Wang, L. Lu, X.-C. Ma, and Q.-K. Xue, Science 340, 167 (2013).
- ³⁵Y.-T. Cui, E. Y. Ma, and Z.-X. Shen, Rev. Sci. Instrum. **87**, 063711 (2016).
- ³⁶X. Wu, Z. Hao, D. Wu, L. Zheng, Z. Jiang, V. Ganesan, Y. Wang, and K. Lai, Rev. Sci. Instrum. 89, 043704 (2018).
- ³⁷ P. Wang, K. Huang, J. Sun, J. Hu, H. Fu, and X. Lin, Rev. Sci. Instrum. 90, 023905 (2019).
- ³⁸T. Quaglio, F. Dahlem, S. Martin, A. Gérardin, C. B. Winkelmann, and H. Courtois, Rev. Sci. Instrum. 83, 123702 (2012).
- ³⁹ M. Lee, B. Kim, S. An, and W. Jhe, Sensors **19**, 2686 (2019).
- ⁴⁰S. Krinner, S. Storz, P. Kurpiers, P. Magnard, J. Heinsoo, R. Keller, J. Lütolf, C. Eichler, and A. Wallraff, EPJ Quantum Technol. 6, 2 (2019).
- ⁴¹ D. Xiao, J. Jiang, J. H. Shin, W. Wang, F. Wang, Y. F. Zhao, C. Liu, W. Wu, M. H. W. Chan, N. Samarth, and C. Z. Chang, Phys. Rev. Lett. **120**, 056801 (2018).
- ⁴²H. Doh and G. S. Jeon, Phys. Rev. B **88**, 245115 (2013).
- ⁴³G. Qiu, P. Zhang, P. Deng, S. K. Chong, L. Tai, C. Eckberg, and K. L. Wang, Phys. Rev. Lett. **128**, 217704 (2022).
- ⁴⁴J. Jiang, D. Xiao, F. Wang, J.-H. Shin, D. Andreoli, J. Zhang, R. Xiao, Y.-F. Zhao, M. Kayyalha, L. Zhang, K. Wang, J. Zang, C. Liu, N. Samarth, M. H. W. Chan, and C.-Z. Chang, Nat. Mater. 19, 732 (2020).